Article

Surface Characterization of P-Type Point Contact Germanium Detectors

Frank Edzards [1,2,*]**, Lukas Hauertmann** [1,2]**, Iris Abt** [1]**, Chris Gooch** [1]**, Björn Lehnert** [3]**, Xiang Liu** [1]**, Susanne Mertens** [1,2]**, David C. Radford** [4]**, Oliver Schulz** [1] **and Michael Willers** [1,2]

1   Max Planck Institute for Physics, Föhringer Ring 6, 80805 Munich, Germany; lhauert@mpp.mpg.de (L.H.); isa@mpp.mpg.de (I.A.); gooch@mpp.mpg.de (C.G.); xliu@mpp.mpg.de (X.L.); mertens@mpp.mpg.de (S.M.); oschulz@mpp.mpg.de (O.S.); mwillers@mpp.mpg.de (M.W.)
2   Department of Physics, Technical University of Munich, Arcisstrasse 21, 80333 Munich, Germany
3   Lawrence Berkeley National Laboratory, 1 Cyclotron Rd., Berkeley, CA 94720, USA; bjoernlehnert@lbl.gov
4   Oak Ridge National Laboratory, 1 Bethel Valley Rd., Oak Ridge, TN 37830, USA; radforddc@ornl.gov
*   Correspondence: edzards@mpp.mpg.de

Abstract: P-type point contact (PPC) germanium detectors are used in rare event and low-background searches, including neutrinoless double beta ($0\nu\beta\beta$) decay, low-energy nuclear recoils, and coherent elastic neutrino-nucleus scattering. The detectors feature an excellent energy resolution, low detection thresholds down to the sub-keV range, and enhanced background rejection capabilities. However, due to their large passivated surface, separating the signal readout contact from the bias voltage electrode, PPC detectors are susceptible to surface effects such as charge build-up. A profound understanding of their response to surface events is essential. In this work, the response of a PPC detector to alpha and beta particles hitting the passivated surface was investigated in a multi-purpose scanning test stand. It is shown that the passivated surface can accumulate charges resulting in a radial-dependent degradation of the observed event energy. In addition, it is demonstrated that the pulse shapes of surface alpha events show characteristic features which can be used to discriminate against these events.

1. Introduction

The observation of neutrinoless double beta ($0\nu\beta\beta$) decay could have major implications on our understanding of the origin of matter in our universe. The decay violates lepton number conservation by two units, and the search for it is the most practical way to ascertain whether neutrinos are Majorana particles, i.e., their own antiparticles ($\nu = \bar{\nu}$). Moreover, together with cosmological observations and direct neutrino mass measurements, it could provide information on the absolute neutrino mass scale and ordering, for recent reviews see [1,2].

One of the most promising technologies to search for $0\nu\beta\beta$ decay are high-purity germanium (HPGe) detectors. Germanium detectors are intrinsically pure, can be enriched to above 92% in the double-beta decaying isotope ^{76}Ge, and provide an excellent energy resolution of about 0.1% FWHM (full width at half maximum) in the region of interest around $Q_{\beta\beta} = 2039$ keV. One particular germanium detector geometry is the so-called p-type point contact (PPC) detector. Due to its large passivated surface separating the readout electrode from the bias voltage electrode, this type of detector is subject to surface effects. In particular, alpha and beta particles hitting the passivated surface can lead to undesired backgrounds. It was already demonstrated that backgrounds induced by alpha particles can be rejected effectively based on the pulse shape of these events [3,4]. For the MAJORANA DEMONSTRATOR experiment it was shown that, based on alpha pulse shape

cuts, the background rate in the region of interest (360 keV window around $Q_{\beta\beta}$) could be reduced from 69.5×10^{-3} cts/(keV · kg · years) to 6.1×10^{-3} cts/(keV · kg · years). This is a reduction of more than one order of magnitude [3]. The energy resolution (2.53 keV FWHM at $Q_{\beta\beta}$) and the detection threshold (sub-keV range) were not affected by applying the cuts [3].

The main objective of this work is to also study the response of PPC detectors to beta particles. The motivation is that these detectors will be redeployed in the first phase of the Large Enriched Germanium Experiment for Neutrinoless $\beta\beta$ Decay (LEGEND), LEGEND-200 [5]. More specifically, it was investigated if surface beta events can be rejected in a similar way as surface alpha events. In addition, the underlying mechanism of PPC detector surface effects was studied in detail. A surface charge model is presented which describes the detector response to surface events. The measurements were complemented by dedicated Monte Carlo simulations which will help to extrapolate the observations from test stands to different detector environments in future double beta decay experiments.

2. PPC Germanium Detectors

PPC germanium detectors are semiconductor detectors with a cylindrical shape, see Figure 1. While the n^+ contact extends over the lateral and bottom detector surface, the p^+ readout contact has the form of a small circular well located at the center of the top surface. The size of the point contact is significantly smaller than that of traditional semi-coaxial detectors. Therefore, PPC detectors have a lower capacitance, typically in the range of 1–2 pF at full depletion, resulting in lower electronic noise and thus in a better energy resolution [6,7]. Moreover, PPC detectors can be operated at lower energy thresholds (<1 keV) which makes them suitable for rare event searches at small energies [3]. Another advantage of this type of detector is the enhanced capability of applying background rejection methods based on so-called pulse shapes. This is due to the specific geometry and arrangement of the electrodes leading to a strong electric field close to the readout contact, and to a relatively low field elsewhere. As a result, the signal shape of events that deposit their energy at a single location (single-site events like $0\nu\beta\beta$ decay events) in the detector is almost independent of the location of the event. This can be used to discriminate these events from events where energy is deposited at multiple sites (multi-site events like Compton-scattered photons) which are a major source of background [8,9].
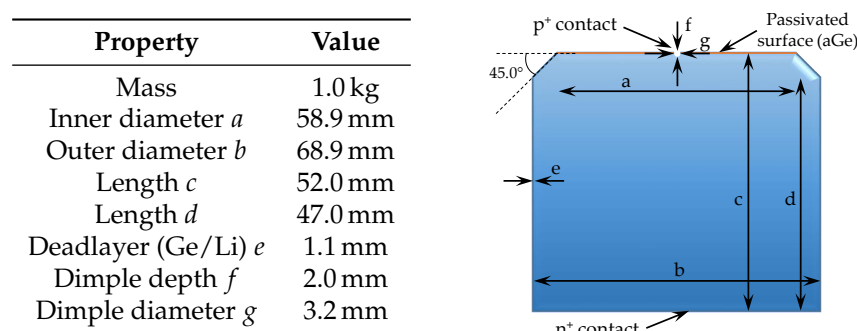
Property	Value
Mass	1.0 kg
Inner diameter a	58.9 mm
Outer diameter b	68.9 mm
Length c	52.0 mm
Length d	47.0 mm
Deadlayer (Ge/Li) e	1.1 mm
Dimple depth f	2.0 mm
Dimple diameter g	3.2 mm

Figure 1. Sketch and parameters of the PPC detector under study.

3. Surface Events as Backgrounds for $0\nu\beta\beta$ Decay Searches

3.1. Alpha Backgrounds

Events induced by alpha particles are a background for ^{76}Ge-based $0\nu\beta\beta$ decay searches. They are predominantly caused by the decay of radon isotopes and their progeny, particularly ^{222}Rn. Radon is a radioactive noble gas which is created naturally as part of the decay chains of uranium and thorium. During the production processing of a germanium detector, it is exposed to air and undergoes various mechanical and chemical treatments. A slight radon contamination of the detector (surface) is unavoidable.

Furthermore, radon contamination and outgassing of parts close to the detectors in the experimental environment can also lead to undesired alpha backgrounds.

In the decay chain of ^{222}Rn, the long-lived isotope ^{210}Po is of major concern. During its decay to the stable isotope ^{206}Pb, an alpha particle with an energy of 5407.5 keV is emitted. If the energy of the alpha particle is degraded, it can lead to a background in the region of interest. The degradation can be caused by the alpha particle loosing energy in the material from which it is emitted, by loosing energy in layers on or close to the detector surface, or by charge trapping or charge loss due to dead regions in the detector. In germanium, the penetration depth of an alpha particle with an energy of $E_\alpha \approx 5$ MeV is of the order of 20 μm.

3.2. Beta Backgrounds

Beta backgrounds are particularly relevant for $0\nu\beta\beta$ decay searches for which detectors are submerged in liquid argon (LAr), such as in LEGEND [10–12]. The long-lived isotope ^{42}Ar ($T_{1/2} = 32.9$ years) is naturally abundant in LAr when sourced from the atmosphere. It is produced by cosmogenic activation and decays via single beta decay to the short-lived daughter ^{42}K ($T_{1/2} = 12.36$ h). The decay energy of $Q_\beta = 599$ keV is too low to create a background event in the region of interest at the $Q_{\beta\beta}$-value of ^{76}Ge. However, subsequent beta decays of the short-lived daughter ^{42}K with a decay energy of $Q_\beta = 3525.4$ keV are a potential source of background.

Within the LAr volume, the path length of beta particles from ^{42}K decays is less than 1.6 cm [13]. Hence, they are only detected if the decay happens in close proximity to the detector surface. Independent of where the beta particles hit the surface, they can lead to background events. However, when impinging on the thick n$^+$ lithium layer, surface beta events have a characteristic signal shape which can be used to discriminate against them [14].

The main difference between alpha and beta particles is their penetration depth into the germanium detector. In contrast to alpha particles, electrons from beta decay penetrate deeper, typically up to several millimeters, depending on their energy. Therefore, not all beta particles show the characteristics of events close to the surface, so-called surface effects.

3.3. Surface Effects and Signal Development

Compared to most other HPGe detector geometries, PPC detectors have a large passivated surface, usually of the order of 30–40 cm^2. This surface extends over the horizontal top surface ($z = 0$ mm) excluding the p$^+$ contact, see Figure 1. Typically, the passivated surface is made from sputtered silicon oxide or amorphous germanium (aGe). This layer has a high resistivity and is left floating, i.e., it is at an undefined electric potential. While the n$^+$ contact is insensitive to surface alpha events (alpha particles cannot penetrate the few mm-thick lithium-drifted layer), beta particles entering through this surface lead to characteristically slow pulses and can be discriminated against. In contrast, the passivated surface and the point contact are highly sensitive to alpha and beta surface events.

Since the passivation layer is left floating, it is susceptible to charge build-up. A non-zero charge on the passivated surface which for example can be induced by nearby materials at non-zero potentials, changes the electric field in the vicinity of this surface and thus affects the signal formation. Without any charge build-up, the electric field lines close to the passivated surface are almost parallel to that surface. However, in the presence of surface charges, the field has a strong perpendicular component, modifying the hole and electron drift paths.

The signal formation of a germanium detector is described by the Shockley–Ramo theorem [15,16]. Any interaction inside the detector creates a cloud of pairs of charge carriers, i.e., holes and electrons. These charge carriers immediately induce positive and negative mirror charges in the electrodes. The holes drift towards the p$^+$ contact, whereas

the electrons drift to the n^+ electrode. For a deposited charge q, the time-dependent signal $S(t)$ in the p^+ contact is given by

$$S(t) = q \left[\mathrm{WP}(\vec{r}_\mathrm{h}(t)) - \mathrm{WP}(\vec{r}_\mathrm{e}(t)) \right], \tag{1}$$

where $\mathrm{WP}(\vec{r}(t))$ denotes the weighting potential at the respective hole (electron) position $\vec{r}_\mathrm{h}(t)$ ($\vec{r}_\mathrm{e}(t)$). The weighting potential of an electrode is determined by the detector geometry and describes how strongly the charge at a given detector position couples to this electrode. For the following discussion, the p^+ contact is the electrode of interest. By definition, the weighting potential on this contact is one, while it is zero on the n^+ contact.

At time $t = 0$, since $\vec{r}_\mathrm{h}(0) = \vec{r}_\mathrm{e}(0)$, the signal is $S(0) = 0$. As the holes approach the p^+ electrode, $\mathrm{WP}(\vec{r}_\mathrm{h}(t))$ increases, see Figure 2a, until the holes are collected at time $t_\mathrm{h}^\mathrm{col}$, and $\mathrm{WP}(\vec{r}_\mathrm{h}(t)) = 1$ for $t \geq t_\mathrm{h}^\mathrm{col}$. As the electrons approach the n^+ electrode, $|\mathrm{WP}(\vec{r}_\mathrm{e}(t))|$ decreases until the electrons are collected at time $t_\mathrm{e}^\mathrm{col}$ and $\mathrm{WP}(\vec{r}_\mathrm{e}(t)) = 0$. As soon as both kinds of charge carriers are collected, only the collected holes determine the signal and $S(t) = q$.
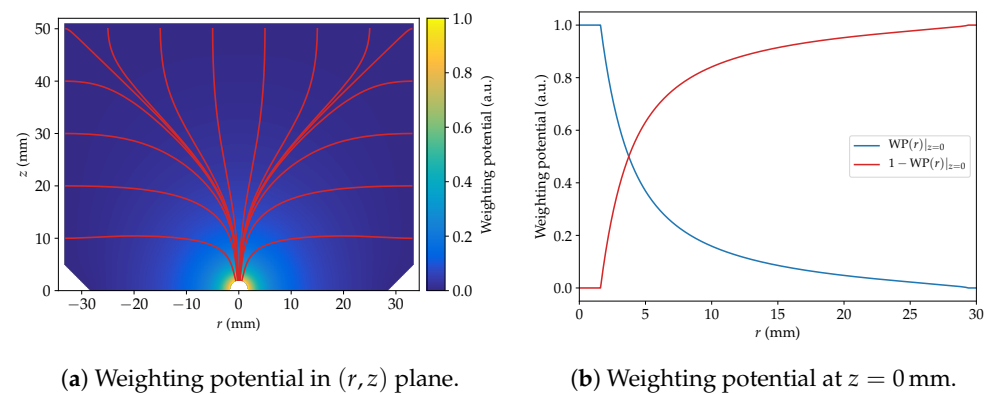

(**a**) Weighting potential in (r, z) plane.   (**b**) Weighting potential at $z = 0$ mm.

Figure 2. (**a**) Weighting potential (WP) of the investigated PPC detector in the (r, z) plane. Red lines indicate the hole drift paths. (**b**) Radial dependence of the WP at the passivated surface ($z = 0$ mm). The WP was simulated using `mjd_fieldgen` [17].

The weighting potential close to the passivated detector surface strongly depends on the radius r. As shown in Figure 2b, the weighting potential $\mathrm{WP}(r)|_{z=0}$ drops quickly with increasing r. The term $1 - \mathrm{WP}(r)|_{z=0}$ shows the opposite behavior, i.e., it increases with radius.

3.3.1. Negative Surface Charges

If the passivated surface carries a negative charge, $\sigma < 0$, holes which are not created in close proximity to the p^+ contact do not drift directly towards the p^+ contact, but are diverted to the surface, see Figure 3a. At the passivated surface, they drift very slowly parallel to this surface in the direction of the p^+ contact. Some holes might even get trapped and stop moving. As a result, the holes are almost stationary and are not collected, at least not within the time in which the signal is recorded. This time is tailored to normal bulk events and is too short to cover the possible collection of delayed holes. Therefore, for times $t \geq t_\mathrm{e}^\mathrm{col}$, i.e., after electron collection, the signal $S(t)$ becomes

$$S(t) \approx q \, \mathrm{WP}(\vec{r}_\mathrm{h}(0)). \tag{2}$$

The larger the radius r, the smaller the final signal amplitude. Due to the presence of negative surface charges, the electrons are repelled from the surface. Simulated electron drift paths are shown in Figure 4a. The paths, which are normally almost parallel to the surface, are modified, i.e., the electrons penetrate deeper into the bulk.
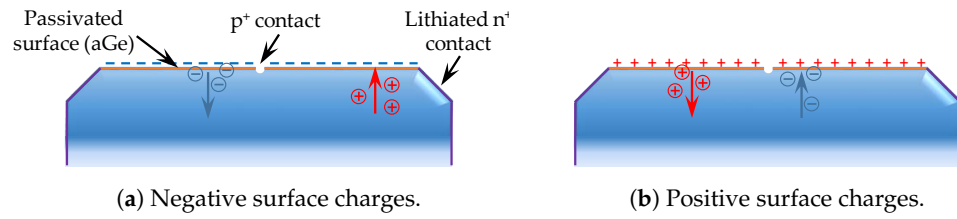
(**a**) Negative surface charges.

(**b**) Positive surface charges.

Figure 3. Effect of (**a**) negative and (**b**) positive charges on the passivated surface of a PPC germanium detector. In the case of negative (positive) surface charges, holes (electrons) are attracted to the surface, whereas electrons (holes) are repelled.
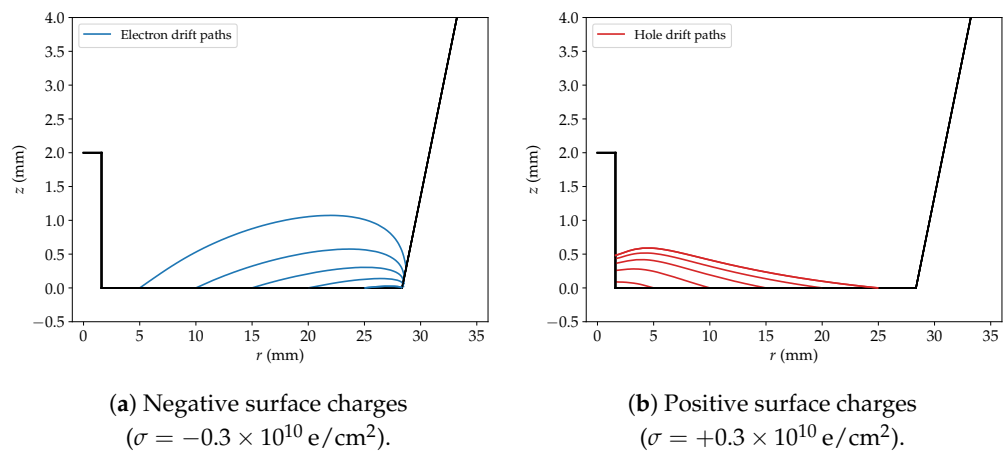

(**a**) Negative surface charges
($\sigma = -0.3 \times 10^{10}\,\text{e}/\text{cm}^2$).

(**b**) Positive surface charges
($\sigma = +0.3 \times 10^{10}\,\text{e}/\text{cm}^2$).

Figure 4. Simulated electron and hole drift paths for (**a**) negative and (**b**) positive charges on the passivated detector surface. The black line indicates the detector contour, the passivated surface is at $z = 0$. The origin of the coordinate system is at the top center of the point contact with the z-axis pointing towards the detector bulk. In the presence of negative (positive) surface charges, the holes (electrons) are attracted to the surface and stop drifting, while the electrons (holes) are repelled into the bulk and do not drift parallel to the surface but inside the bulk towards the respective contacts. The drift paths were simulated using `mjd_siggen` [17].

3.3.2. Positive Surface Charges

For a positive charge on the passivated detector surface, $\sigma > 0$, the electrons created during a particle interaction are attracted to the surface, whereas the holes are repelled, see Figure 3b. The drift paths of the holes are modified as shown in Figure 4b. In this case, the electrons are almost stationary and are not collected during the time in which the signal is recorded. Thus, for times $t \geq t_\text{h}^\text{col}$, i.e., after hole collection, the signal becomes

$$S(t) \approx q\left[1 - \text{WP}(\vec{r}_\text{e}(0))\right]. \tag{3}$$

The larger the radius r, the larger the final signal amplitude.

3.3.3. Impact of Surface Charges on Alpha and Beta Events

For both, negative and positive charges on the passivated detector surface, the signal amplitude is reduced. After the application of the standard calibration, the signal becomes the observed energy E^obs. In both cases, E^obs is smaller than the true event energy E^true. The radial dependence of E^obs allows to distinguish experimentally between the two cases.

Due to the small penetration depth of alpha particles in germanium, it is expected that basically all charge carriers are affected by the surface effects described above. Thus, in the case of negative surface charges, it is expected that E^obs approximately follows the radial dependence of the weighting potential. The expected signal development for a homogeneously distributed surface charge ($\sigma = -0.3 \times 10^{10}\,\text{e}/\text{cm}^2$) at varying radii is

shown in Figure 5. Point-like normalized charges created at $z_0 = 16\,\mu m$ were used in the simulation. Holes created very close to the p^+ contact are collected quickly. However, the negative charge induced by the electrons still close to the p^+ contact reduces the signal amplitude. The electrons drift away from the p^+ contact and the effect is shown as a positive contribution. At $r = 2\,mm$, the holes are fully collected and when the electrons have reached the n^+ contact, the signal is $S(t) = 1$. At higher radii, the holes are not collected and their signal contribution is constant from $t = 0$ on. Only the negative contribution to the signal from the electrons becomes smaller as the electrons drift. Again, this is shown as a positive contribution being almost identical to $S(t)$ which reaches its final value of $\mathrm{WP}(\vec{r}_h(0))$ at time t_e^{col}, cf. Equation (2). Consequently, the observed energy E^{obs} follows the radially declining weighting potential.
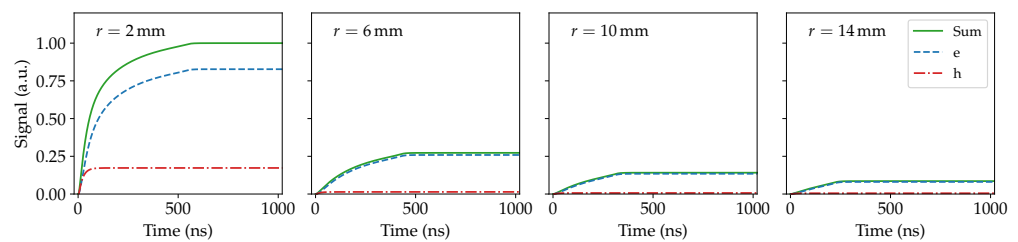

Figure 5. Simulated development of the alpha event signals in the presence of negative charges on the passivated detector surface ($\sigma = -0.3 \times 10^{10}\,e/cm^2$) for selected radial positions. Point-like charges were started at a depth of $z_0 = 16\,\mu m$. The components from holes (h) and electrons (e) are discussed in the text. The waveforms were simulated using `mjd_siggen` [17].

3.4. Delayed Charge Recovery

Delayed charge recovery (DCR) describes the phenomenon of an extra slow charge collection component for surface alpha events [3,4,18]. In the last section, the drift velocity of one kind of charge carriers was assumed to be too low to observe charge collection. DCR reflects that at least some part of the affected charge carriers are collected within the time of signal recording. Compared to events in the detector bulk (e.g., gamma events), the presence of a DCR component for surface alpha events modifies the tail of the signal pulse. As shown in Figure 6, the tail of the pole-zero-corrected waveform (this correction addresses the decay of the signal in a charge sensitive amplifier) still increases after the charge collection in the detector bulk can be assumed to be completed. In contrast, for a gamma event with the same energy in the detector bulk, the tail stays at a constant value. The distinct DCR feature in the waveform makes the DCR effect an effective tool to identify and reject surface alpha events on the passivated surface of PPC detectors. There are two mechanisms that can potentially explain the delayed collection of charges for surface alpha events:

1. A certain fraction of charges created during the alpha interaction is trapped in a $\mathcal{O}(\mu m)$-thick region at or near the passivated surface. In this case, the DCR effect corresponds to a slow release of these charges into the detector bulk (with a certain release time τ_r) and their subsequent drift to the electrodes.
2. Charges created on or close to the passivated surface have a significantly reduced drift velocity compared to the drift velocity in the detector bulk [19]. In this case, the DCR effect corresponds to a slow drift of charges along the passivated surface.

Typically, the charge drift along the passivated surface takes much longer than the time, in which the waveforms are digitized. Until recently, it was assumed that the main component leading to DCR is due to the trapping and the subsequent slow release of charges at the passivated surface. In previous measurements, a charge release time on the order of several microseconds was observed. In addition, the fraction of charge released into the detector bulk was on the order of a few percent [4,18]. However, pulse shape

simulations including the effects of diffusion and self-repulsion have demonstrated that surface drifts can also have an impact, cf. Section 5.3.1.
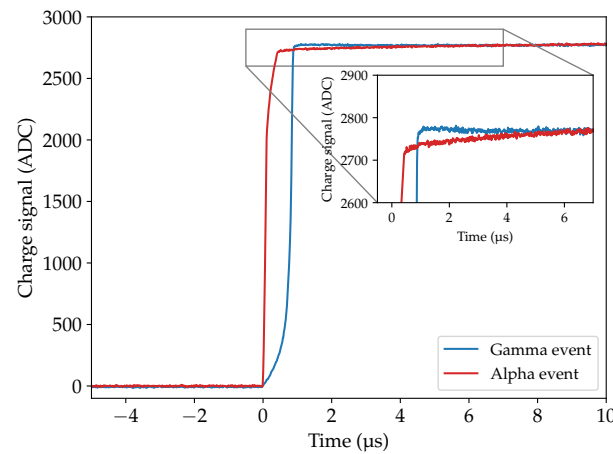

Figure 6. Typical examples of a bulk gamma event (blue curve) and of a surface alpha event (red curve) with the same energy. The waveforms were recorded using the PPC detector under study. The baseline and pole-zero-corrected alpha signal features a slowly rising tail (see inset). This component can be explained as due to DCR. Due to its proximity to the signal readout electrode, the rise time of the surface alpha event is shorter (steeply rising leading edge) than the rise time of the gamma bulk event.

The DCR effect can be exploited to define a tail-based pulse shape discrimination parameter, the DCR rate parameter. It is computed by estimating the slope δ of the pole-zero-corrected waveform tail based on a two-point slope estimate [3,4]:

$$\delta = \frac{y_1 - y_2}{t_1 - t_2}. \tag{4}$$

Here, y_1, y_2 denote average signal values, and t_1, t_2 average time values. The time values correspond to the average values in the intervals

$$\text{I)} \ t_{97\%} + 2\,\mu s \leq t \leq t_{97\%} + 3\,\mu s, \tag{5}$$

$$\text{II)} \ t_{\text{last}} - 1\,\mu s \leq t \leq t_{\text{last}}, \tag{6}$$

where $t_{97\%}$ is the time, at which the waveform has reached 97% of its maximum amplitude, and t_{last} is the time corresponding to the last sample of the waveform trace. These time windows have been chosen to allow comparisons with the measurement results presented in [3,4,18]. However, it should be noted that this definition introduces a slight dependence on the trigger time in the waveform trace: The second window is not defined relative to the onset of the charge collection, but rather comprises a fixed window (last microsecond of the waveform trace).

4. Measurements

4.1. Experimental Setup

The PPC detector surface characterization measurements presented in this work were carried out in the GALATEA (GermAnium LAser TEst Apparatus) facility, a fully automated multi-purpose scanning test stand that was built to investigate bulk and surface effects of HPGe detectors [20,21]. Due to its versatility, it allows for almost complete scans of the detector surface with alpha, beta, and gamma radiation.

The facility is a large customized vacuum cryostat housing the scanning stages, the germanium detector, the radioactive source(s), and the signal readout electronics. The detector under investigation can be mounted in an aluminum or a copper holding structure which is also used for its cooling. The detector is shielded against infrared (IR) radiation by a cylindrical copper hat. The IR shield has two slits (one on the side of the hat, one on top), along which the collimators with the radioactive sources are guided during the measurements. A system consisting of three independent stages allows an almost complete scan of the detector surface. One stage can rotate the IR shield up to 360° with respect to the detector, facilitating azimuthal scans. The additional two linear stages are used to move the top collimator across the top surface for top scans, and the side collimator vertically for side scans.

The detector used for this work, see Figure 1, is a PPC germanium detector with natural isotopic composition and properties that closely resemble those of the detectors previously operated in the MAJORANA DEMONSTRATOR [3,22]. To allow for a scan of the passivated surface, the detector was installed with the point contact facing up in a customized detector mount, see Figure 7. The n^+ electrode was connected to the high voltage module via a spring-loaded pin located at the detector bottom. Likewise, connection to the p^+ contact was established with a pogo pin which was attached to a narrow PTFE bar mounted on top of the detector. In addition, the PTFE holding structure was used to guide the signal cable.
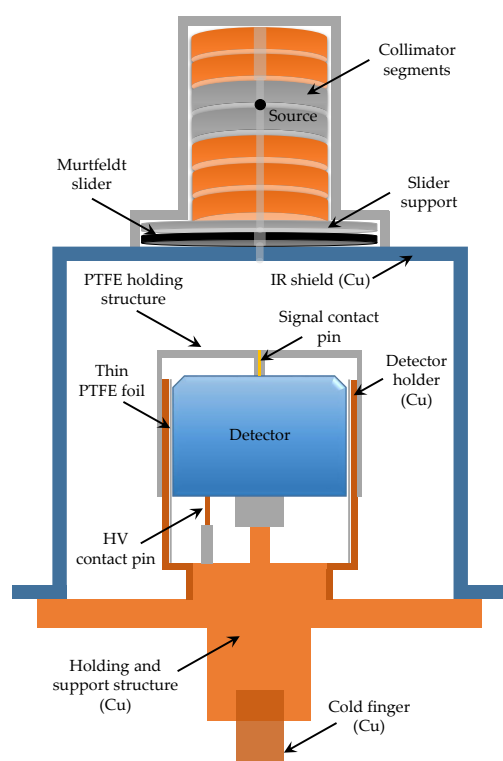

Figure 7. Sectional view of the PPC detector installed in the GALATEA test facility. The detector is mounted in a copper structure that is cooled via liquid nitrogen. It is surrounded by a copper IR shield. For the scan measurements presented in this manuscript, the detector top surface was irradiated by a radioactive source installed in the top collimator above the IR shield. For reasons of visual clarity, the side collimator of GALATEA, not relevant for this work, is not shown.

Data were acquired with a Struck 14-bit SIS3316 flash ADC (FADC) digitizing the analog signals from the charge sensitive amplifier with a sampling frequency of 250 MHz. For every signal, 5000 samples corresponding to a total waveform trace length of 20 µs were recorded.

4.2. Characterization of Surface Alpha Interactions

4.2.1. Source Configuration

For the PPC detector surface characterization with alpha particles, an ^{241}Am source with an activity of $A_0 = 40\,\mathrm{kBq}$ and an expected FWHM of $\sim$19 keV at the 5.5 MeV alpha peak was mounted in the top collimator of GALATEA. Suitable cylindrical PTFE and copper segments were used to fill the collimator frame. Based on the collimator geometry and the source strength, an alpha rate of $\sim$0.7 counts/s was expected at the detector top surface. In all measurements, the ^{241}Am beam spot had an incidence of 90° on the detector surface. In close vicinity to the point contact, the beam spot was shadowed by the PTFE bar. Hence, it was not possible to take data in this region. An uncollimated ^{228}Th source ($A_0 = 100\,\mathrm{kBq}$) was additionally mounted on top of the IR shield for energy calibration purposes, and to confirm pulse shape discrimination capabilities.

Several radial scans at different azimuthal positions, as well as background and stability measurements were conducted. For the radial scans, a measurement time of 2 h at each scan point provided sufficiently high statistics. The detector was operated at a bias voltage of $V_B = 1050\,\mathrm{V}$.

4.2.2. Results

The radial response of the PPC detector to surface alpha events is of special interest. The energy spectra of a measurement with the ^{241}Am source at $r = 5\,\mathrm{mm}$, and of a measurement with only the ^{228}Th source present are shown in Figure 8. The contribution from the ^{228}Th source dominates the energy spectrum up to $\sim$2.6 MeV. At higher energies, the measurement with the ^{241}Am source deviates from the ^{228}Th-only measurement. The higher count rate is attributed to alpha events. To isolate these events from other events, radius-independent multivariate cuts were developed [23]. More specifically, cuts on various pulse shape parameters were used to exclude regions in the parameter space which did not contain alpha events.
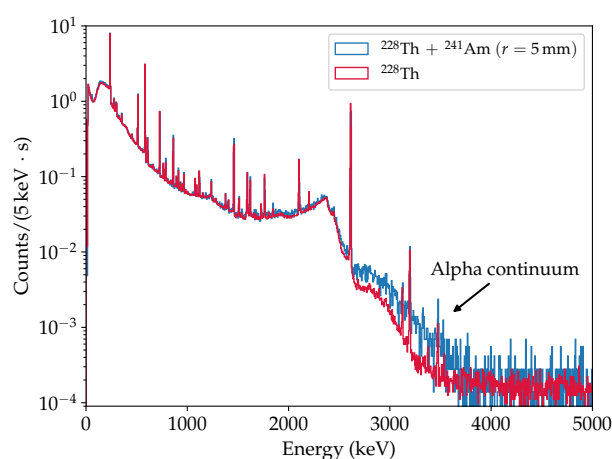

Figure 8. Energy spectra as measured with the ^{228}Th and the ^{241}Am source at the position $r = 5\,\mathrm{mm}$ (blue curve), and the ^{228}Th source only (red curve). At higher energies, a continuum of alpha events is visible.

Dependence of the Observed Energy on the Radius

To quantify the dependence of the observed energy E_α^{obs} on the radius r for surface alpha events, the energies of the events in the alpha-enriched regions were histogrammed and corrected for background events, see Figure 9a. At small r, the alpha events form a broad distribution with relatively high E_α^{obs}. As r increases, the distribution becomes narrower and shifts to lower values E_α^{obs}. A quantitative description of this degradation was obtained by extracting the mean alpha energies $\langle E_\alpha^{\mathrm{obs}} \rangle$ from the distributions. The ranges of E_α^{obs} were constrained manually to reject remaining background events. The mean alpha

energies $\langle E_\alpha^{\mathrm{obs}} \rangle$ as a function of r for two radial ^{241}Am scans at different azimuthal positions are shown in Figure 9b. At the outermost radii, $\langle E_\alpha^{\mathrm{obs}} \rangle$ is strongly reduced, i.e., almost no charges are collected. In contrast, at small r, the mean energy is $\langle E_\alpha^{\mathrm{obs}} \rangle > 2500$ keV. The results of the two measurements are in good agreement. The observed reduction of the mean alpha energy is consistent with the presence of negative surface charges on the passivation layer, cf. Section 3.3. These charges trap the holes created during the interaction, reducing the signal amplitude. The broadness of the peak at low r is partly influenced by the size of the beam spot. However, the total width also includes some stochastic effect. Between the two scans, the detector was unbiased and the cryostat was re-evacuated. This did not affect the observations significantly.
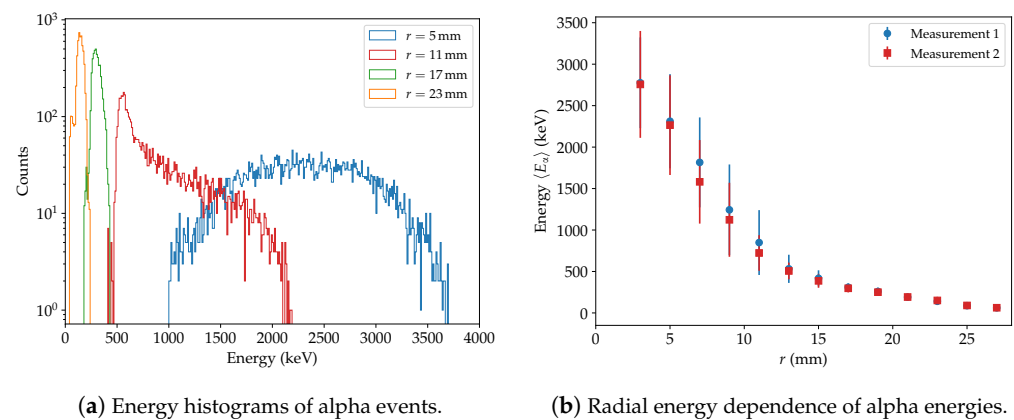

(**a**) Energy histograms of alpha events. (**b**) Radial energy dependence of alpha energies.

Figure 9. Radial dependence of the observed energy of alpha events: (**a**) Energy spectra of the alpha populations at selected radial positions after the application of multivariate cuts. (**b**) Mean observed alpha energy $\langle E_\alpha^{\mathrm{obs}} \rangle$ as a function of radius r for two radial ^{241}Am scans at different azimuthal positions. Error bars represent the standard deviations of the constrained E_α^{obs} distributions. The measurements were conducted with the detector operated at a bias voltage of $V_{\mathrm{B}} = 1050$ V.

Even though $\langle E_\alpha^{\mathrm{obs}} \rangle$ strongly depends on r, alpha events were not lost. This could have occurred for a locally increasing dead layer. However, the total number of alpha events as a function of r remained almost constant at a value of about 5000 events per scan position, see Figure 10. The deviation at small radii is most likely due to a partial shadowing of the ^{241}Am beam spot by the PTFE bar. The decreasing alpha rate at the outer radii can be explained by the fact that the alphas hit the lithiated layer of the taper which they cannot penetrate. The plot also shows the alpha counts as predicted by GEANT4 simulations. They agree very well with the measurement. The plateau as well as the drop of the event rate at the center and at the edge of the detector are well described by the simulations. However, a small offset of 3 mm was observed. This was found to be due to a corresponding slight offset between the center of the detector and the central position of the collimator. The r values for the data were corrected for this offset.

Radial DCR Dependence

The DCR effect is, in general, an effective way to identify surface alpha events. To investigate its radial dependence, the DCR rate parameter was computed for every event as described in Section 3.4. The resulting distributions as a function of energy are shown in Figure 11. It can be observed that bulk events have DCR values around zero, whereas surface alpha events can be identified as events with values DCR > 0. With increasing r, the DCR value decreases. In the next step, the DCR rates were histogrammed, corrected for background events, and the mean DCR rates $\langle \mathrm{DCR_r} \rangle$ were extracted from the distributions. The dependence of $\langle \mathrm{DCR_r} \rangle$ on r for two radial ^{241}Am scans at different azimuthal positions is shown in Figure 12a. Comparable to the mean alpha energy $\langle E_\alpha^{\mathrm{obs}} \rangle$, $\langle \mathrm{DCR_r} \rangle$ decreases considerably with increasing r. At $r > 15$ mm, the mean DCR rate of surface alpha events

is close to zero. This means that in this region alpha events are no longer distinguishable from bulk events.
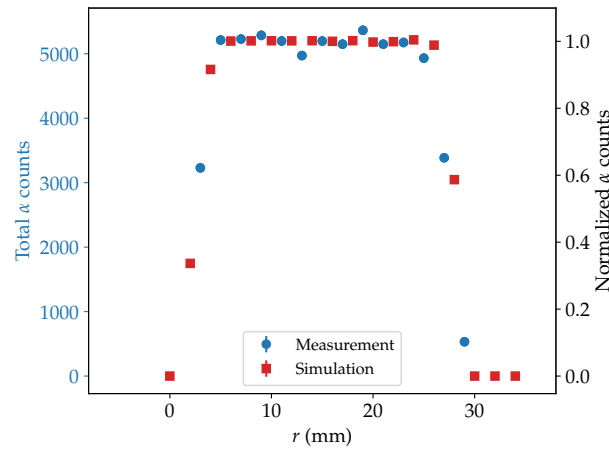

Figure 10. Dependence of the number of recorded alpha events on the radius r. Predictions from GEANT4 simulations are also shown.
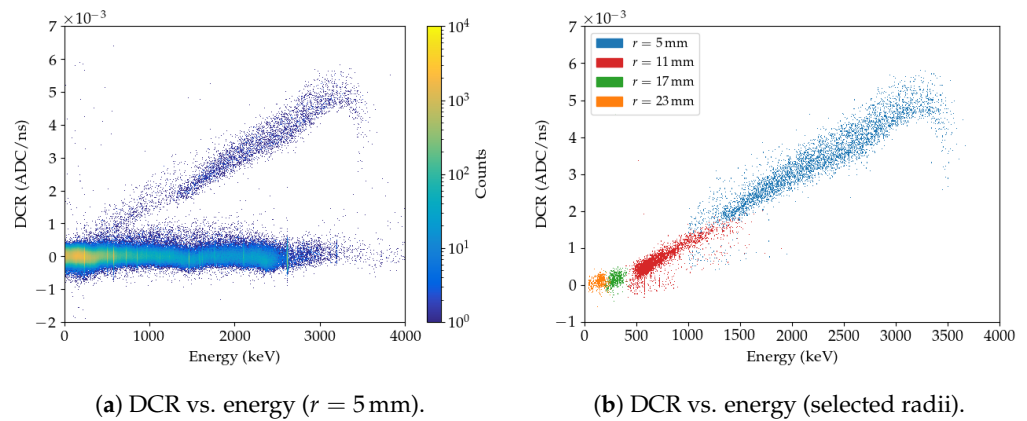

(**a**) DCR vs. energy ($r = 5\,\text{mm}$).   (**b**) DCR vs. energy (selected radii).

Figure 11. (**a**) Scatter plot of DCR vs energy at $r = 5\,\text{mm}$. While bulk events have DCR values centered around zero, surface alpha events have values DCR > 0. (**b**) Multivariate cuts are used to isolate surface alpha events. With increasing radius, the DCR value of surface alpha events decreases.
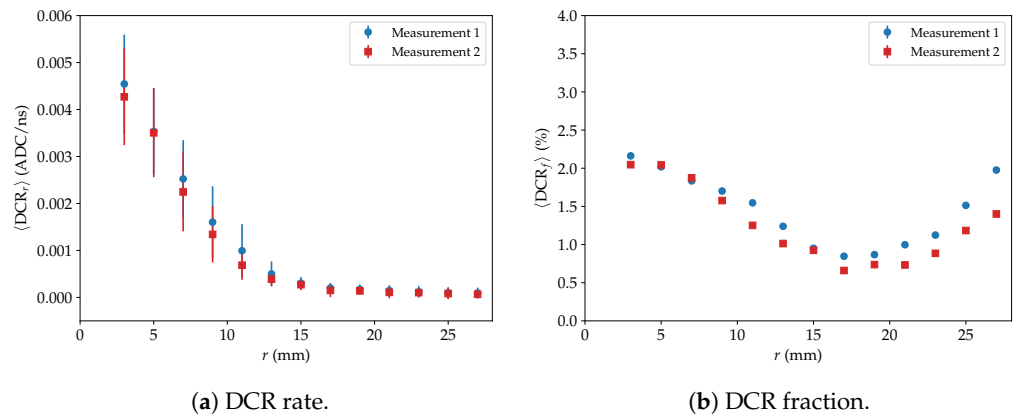

(**a**) DCR rate.   (**b**) DCR fraction.

Figure 12. Radial dependence of (**a**) $\langle \text{DCR}_r \rangle$ and (**b**) $\langle \text{DCR}_f \rangle$ for two radial ^{241}Am scans at different azimuthal positions. Error bars represent the standard deviations of the DCR distributions.

Another way of quantifying the DCR effect is to convert the mean DCR rate $\langle \text{DCR}_r \rangle$ to an average DCR fraction $\langle \text{DCR}_f \rangle$, which is defined as $\langle E_\alpha^{\text{ex}} \rangle / \langle E_\alpha^{\text{obs}} \rangle$, where $\langle E_\alpha^{\text{ex}} \rangle$ is

the amount of additionally observed energy due to DCR. This extra observed energy is calculated by converting the mean DCR rate from ADC/ns to keV/ns units and integrating over the length of the waveform tail $\Delta t \approx 14\,\mu s$. The radial dependence of $\langle DCR_f \rangle$ is shown in Figure 12b. The value of $\langle DCR_f \rangle$ drops with increasing r from about 2% to about 0.5% at $r \approx 15\,mm$, where the value of the mean DCR rate approaches zero. At higher r, $\langle DCR_f \rangle$ seems to increase again. However, it should be noted that these fractions are numerically problematic as also $\langle E_\alpha^{obs} \rangle$ approaches zero, see Figure 9b.

4.3. Characterization of Surface Beta Interactions

4.3.1. Source Configuration

For the surface characterization measurements with beta particles, a ^{90}Sr source with an activity of $A_0 = 5.0\,MBq$ was mounted in the top collimator. Suitable cylindrical tungsten segments were used to fill the collimator frame. Based on the collimator geometry and the source strength, an electron rate of ~300 counts/s was expected at the detector surface. In all measurements, the ^{90}Sr beam spot had an incidence of 90° on the detector surface.

As for the surface characterization measurements with alpha particles, several radial scans at different azimuthal positions, as well as background and stability measurements were conducted. In contrast to the alpha measurement configuration, no radial offset between the center of the detector and the central position of the collimator was observed for the beta measurements: The detector holding structure and the collimator were readjusted between the measurement campaigns. Typically, a measurement time of 0.5 h per scan point was chosen. The measurements were conducted with the detector operated either at the bias voltage of $V_B = 1050\,V$ or at $V_B = 2000\,V$. The focus of the analysis is on the data obtained at the higher bias voltage. Less pronounced results were obtained for the data taken with the lower bias voltage. The observed small dependence on the bias voltage is not yet fully understood.

4.3.2. Results

Dependence of the Observed Energy on the Radius

First, the energy spectra recorded in the presence of the ^{90}Sr source were corrected for background events, see Figure 13. The plot shows that the distribution of E_β^{obs} strongly depends on the radius r. In particular, the following two effects can be observed:

(1) The total number of events decreases with increasing radius r.
(2) The energy continuum E_β^{obs} shifts to lower energies with increasing r. This is especially pronounced around the endpoint of the distribution.
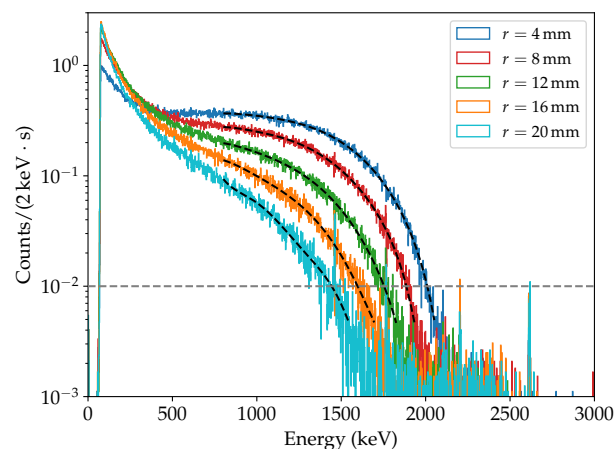

Figure 13. Background-subtracted energy spectra E_β^{obs} of a radial ^{90}Sr scan. The black dashed lines correspond to polynomial fits to the spectra. The endpoint was approximated by determining the intersection of the fits with a fixed value (grey dashed line).

The first effect was quantified by calculating the total count rate as integrated over the entire energy range (0–3 MeV) as a function of r, see Figure 14a. The count rate first increases and then decreases with r. The reduced rate at small r is due to the partial shadowing of the beam spot by the PTFE bar. While the event rate for alpha events was almost constant, the reduced event rate at higher radii shows that some of the beta electrons are completely lost. This is most likely an experimental artefact: As the activity of the ^{90}Sr source was higher than the activity of the ^{241}Am source, the trigger threshold of the data acquisition system had to be increased from $\sim$16 keV to $\sim$50 keV to prevent too high a rate of pile-up events. Therefore, events which were affected severely by surface effects and thus with too small E_β^{obs} were not recorded.

The dependence of the spectral endpoint on r was investigated by fitting the energy spectra with a seventh-order polynomial, see Figure 13. The endpoints E_0^{obs} were approximated by determining the energies, at which the fit functions drop to a fixed value of 10^{-2} counts/$(2 \text{ keV} \cdot \text{s})$. This value was chosen to avoid statistical fluctuations at smaller count rates. As the estimate of the endpoints is rough and since this method is affected by binning effects, normalized endpoints $E_0 = E_0^{\text{obs}}/\max(E_0^{\text{obs}})$ are shown in Figure 14b. The value of E_0 decreases significantly with r. This is in good qualitative agreement with the behavior of E_α^{obs} as described in Section 4.2. In particular, the results are again consistent with the presence of negative charges on the passivated detector surface.
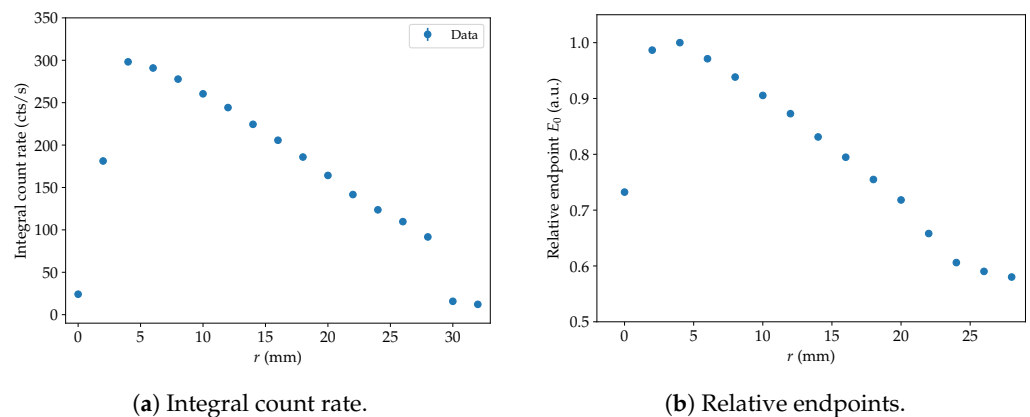

(**a**) Integral count rate.   (**b**) Relative endpoints.

Figure 14. (**a**) Dependence of the integral count rate and (**b**) of the relative endpoint on r as observed for a ^{90}Sr scan. The measurements were conducted with the detector operated at a bias voltage of $V_{\text{B}} = 2000$ V.

Radial Dependence of Other Pulse Shape Parameters

The radial dependence of other pulse shape parameters and their correlations were also investigated. Two event populations were identified by studying the correlation between the drift time and the energy E_β^{obs}. The drift time is defined as the time period in which 90% of the total signal height is reached. The correlations for selected radii are shown in Figure 15.
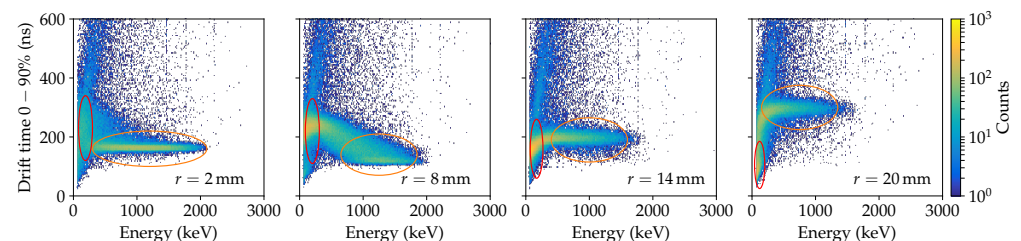

Figure 15. Correlations between the drift time (0–90%) and E_β^{obs} at selected r. The red vertical and orange horizontal ellipses in the distributions indicate two event populations.

One population, indicated by vertical ellipses, is located at small energies and its drift times decrease with increasing r. The second population, indicated by horizontal ellipses, is located at higher energies and its drift times increase with r. With the help of pulse shape simulations it can be shown that the first population corresponds to events with a small penetration depth, which are sensitive to surface effects. For the observed negative charges on the passivated detector surface, the signal development is driven by the collection of electrons while the holes are almost stationary and provide an almost constant contribution. Since at higher r the electrons are closer to the n$^+$ contact, their drift time decreases. As the weighting potential at higher r is small, E_β^{obs} is small for these events. The second population corresponds to events with higher penetration depths which are mostly insensitive to surface effects. These interactions are subject to the usual charge collection behavior, i.e., the holes are at least partially collected and E_β^{obs} is closer to the true energy of the incident electrons. Since at higher r, the holes have a longer drift path to the p$^+$ readout contact, the drift time increases with r. These separated two event populations show that, unlike alphas, not all beta electrons are affected significantly by surface charges. Only events where the electrons do not penetrate deeply are strongly affected.

5. Pulse Shape Simulations

To better understand the measurement results discussed above, dedicated surface event simulations were performed. To this end, the package `Siggen` consisting of the two programs `mjd_fieldgen` and `mjd_siggen` was used [17].

Electric Field and Weighting Potential

The stand-alone program `mjd_fieldgen` was used to calculate the electric potential, the electric field, and the weighting potential inside the detector. The computation is based on a numerical relaxation algorithm on an adaptive grid. For PPC detectors, due to their cylindrical symmetry, the computation can be performed on a two-dimensional grid (coordinates: r and z). At the passivated detector surface, a reflective symmetry is used as a boundary condition for the relaxation algorithm. This is in accordance with the requirement that for zero surface charge at the passivation layer, the field lines close to the surface are parallel to that surface, such that no charges pass the surface [7].

Signal Formation

The signals corresponding to energy depositions at specific locations in the detector can be simulated with `mjd_siggen`. The program combines the field maps generated with `mjd_fieldgen` with a charge drift model containing information on the electron and hole mobilities to compute the charge drift path [24]. Furthermore, the corresponding signal is calculated according to the Shockley–Ramo theorem, cf. Equation (1).

Both programs require a number of user inputs that are read in from a common configuration file. These inputs include the detector geometry and configuration (bias voltage, temperature), the impurity profile, and other settings (initial grid size, charge cloud size, electronics response, etc.). Most importantly for this work, a (homogeneously distributed) surface charge can be added to the passivated detector surface. The surface charge is expressed in units of e/cm^2 and is added as an impurity at every grid point on the surface.

5.1. Influence of Surface Effects on Pulse Shape Parameters

Pulse shape parameter maps were calculated to study the impact of surface effects on important quantities such as the energy E^{obs}, drift time, etc. To this end, point charges with starting positions arranged in a finely meshed grid in the (r, z) plane were simulated using `Siggen`. The effects of diffusion and self-repulsion were not included in the simulations, cf. Section 5.3.1. The parameter maps for negative and positive surface charges ($\sigma = \pm 0.3 \times 10^{10}$ e/cm^2) for the quantities energy fraction $E^{\text{obs}}/E^{\text{true}}$, A/E, and drift time (0–90%) are shown in Figure 16. The A/E parameter describes the ratio of the maximum

amplitude of the current pulse (A), and the amplitude (energy) of the charge pulse (E^{obs}). It is commonly used to discriminate background events from signal events. More information on this pulse shape parameter and its determination can be found in [8,25].
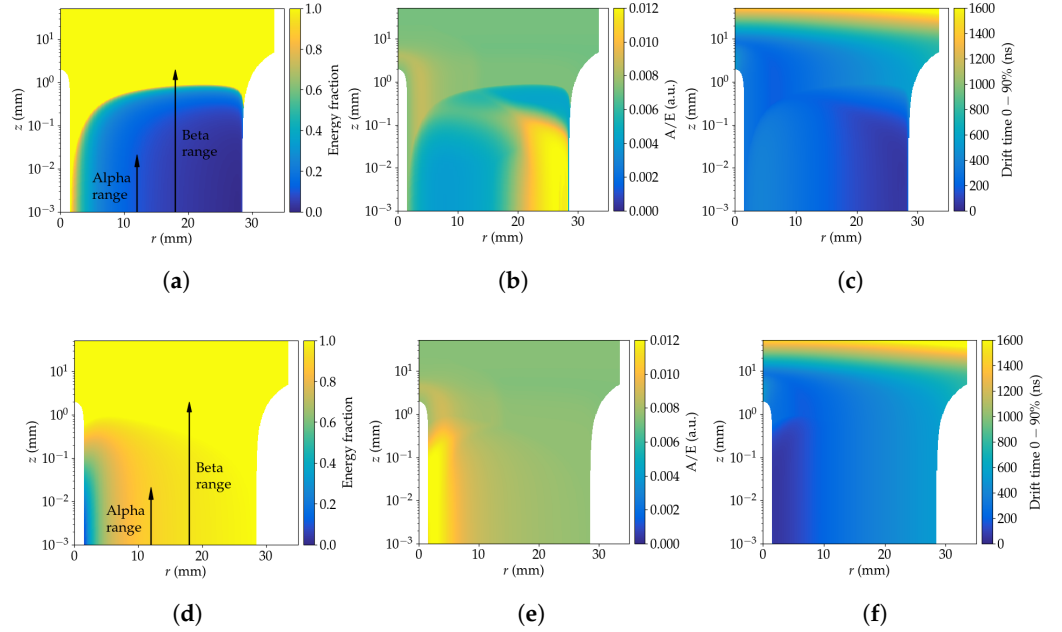

Figure 16. Pulse shape parameter maps of the quantities energy fraction $E^{\mathrm{obs}}/E^{\mathrm{true}}$, A/E, and drift time (0–90%) for a negative surface charge ($\sigma = -0.3 \times 10^{10}\,\mathrm{e}/\mathrm{cm}^2$, top row), and for a positive surface charge ($\sigma = +0.3 \times 10^{10}\,\mathrm{e}/\mathrm{cm}^2$, bottom row) at a bias voltage of $V_{\mathrm{B}} = 1050\,\mathrm{V}$. The distributions are shown with a logarithmic scale in z to highlight surface effects at the passivation layer. The typical ranges of alpha and beta particles within the active detection volume are indicated by the arrows. (**a**) $E^{\mathrm{obs}}/E^{\mathrm{true}}$, $\sigma < 0$. (**b**) A/E, $\sigma < 0$. (**c**) Drift time (0–90%), $\sigma < 0$. (**d**) $E^{\mathrm{obs}}/E^{\mathrm{true}}$, $\sigma > 0$. (**e**) A/E, $\sigma > 0$. (**f**) Drift time (0–90%), $\sigma > 0$.

The energy fraction parameter maps ($E^{\mathrm{obs}}/E^{\mathrm{true}}$) for negative and positive surface charges show that in most of the active detection volume, the true event energy is obtained, i.e., $E^{\mathrm{obs}} \approx E^{\mathrm{true}}$. However, for $\sigma < 0$, there is a strong reduction of E^{obs} in a region close to the passivated surface ($z \lesssim 1\,\mathrm{mm}$). In this region, holes created during an interaction are attracted to the surface and become quasi-stationary. The signal development is driven by the drift of electrons to the n$^+$ contact, cf. Section 3.3. At $z \lesssim 1\,\mathrm{mm}$, the energy fraction $E^{\mathrm{obs}}/E^{\mathrm{true}}$ decreases for increasing r. Surface alpha events with typical penetration depths of tens of micrometers are fully contained in this region of reduced E^{obs}. In contrast, surface beta events which have in average higher penetration depths of up to a few millimeters, are only partially affected.

In the case of positive surface charges, $\sigma > 0$, there is only a small region in the vicinity of the point contact where events have a strongly reduced E^{obs} and thus small $E^{\mathrm{obs}}/E^{\mathrm{true}}$ values. Here, electrons created during an interaction are attracted to the passivated surface and become quasi-stationary. The signal development is driven by the drift of holes to the p$^+$ contact. At $z \lesssim 1\,\mathrm{mm}$, the reduction of E^{obs} gets less severe with increasing r. Compared to the case of a negative surface charge build-up, the reduction of E^{obs} is much less pronounced. For increasing absolute surface charge $|\sigma|$ (at fixed bias voltage) or decreasing bias voltage (at fixed surface charge), the regions of reduced E^{obs} extend towards higher depths z.

The A/E map for a negative surface charge shows that for $z \lesssim 1\,\mathrm{mm}$, the A/E values first slightly decrease and then strongly increase with increasing r. This can be explained by the fact that at larger r, the electrons drift in a slowly changing weighting field for a short drift time which results in fast signals and thus high A/E values. For positive surface

charges, high A/E values are encountered in the region close to the point contact. Here, the holes drift in a rapidly changing weighting field for a short drift time which also results in fast signals.

The drift time of events in the region of reduced E^{obs} for $\sigma < 0$ decreases with increasing r. This is due to the closer proximity of the electrons to the n$^+$ electrode at higher r so they are collected faster. The drift time map also shows that at higher penetration depths ($z \gtrsim 1$ mm), the drift time increases with increasing r. Here, the holes are collected and their drift times drive what is measured. At larger r, they have a longer drift path to the p$^+$ contact, and therefore a longer drift time. Likewise, for positive surface charges, where the signal formation in the region of reduced E^{obs} is driven by the collection of holes, the drift time increases with radius.

5.2. Full Monte Carlo Simulations

An extensive simulation campaign was carried out to better understand the results obtained in the surface characterization measurements with alpha and beta particles. First, realistic energy deposition distributions in the PPC detector were simulated using the toolkit GEANT4. Second, the corresponding signals were simulated using Siggen. Third, various pulse shape parameters were computed and analyzed in post-processing routines. This three-step procedure is illustrated schematically in Figure 17.
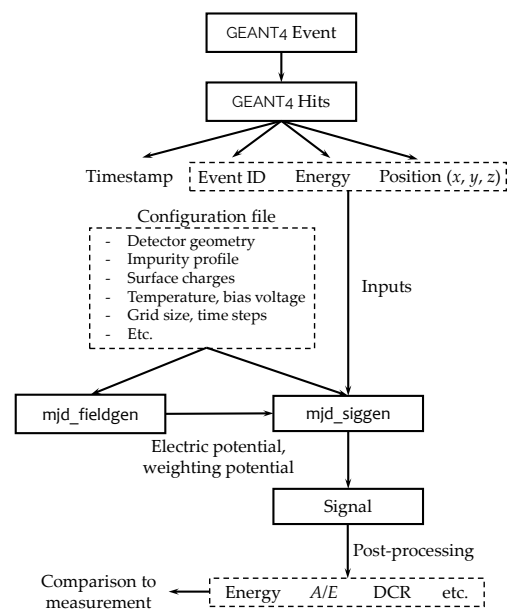

Figure 17. Flow diagram of the surface event simulations.

(1) GEANT4 simulations

In the first step, the interaction positions and energy depositions of surface alpha and beta events in a PPC germanium detector were simulated using GEANT4. To this end, a simplified geometry of the GALATEA scanning facility was implemented. To acquire sufficiently high statistics, several million events were simulated. For every simulated event, the parameters timestamp, event ID, energy E^{true}, and position (x, y, z) were stored for every charge deposition (hit) in the detector.

(2) Pulse shape simulations

The outputs of the GEANT4 simulations were used as an input for pulse shape simulations with Siggen. For a given event, the signals corresponding to the individual hits were simulated and finally summed up to form the signal (weighted with the individual E^{true}). The evolution of the charge cloud size due to diffusion and self-repulsion was neglected in all simulations. This will be discussed in more detail in Section 5.3.1. Moreover, the

implementation of a sophisticated electronic response model (e.g., modeling the electronic noise) was omitted. The simulated waveform of every event was stored for a time period of 1500 ns (starting at $t = t_0 = 0$ ns) for time steps of $\Delta t = 1$ ns. This trace length was chosen to minimize the computing time while ensuring the simulation of the full signal for events close to the passivated detector surface.

(3) Post-processing

In post-processing, several pulse shape parameters were extracted from the simulated waveforms. These include the observed energy E^{obs}, the maximum current amplitude to estimate A/E, the signal drift and rise time, and the DCR rate. The DCR effect for surface alpha events was modeled by convolving the current signal with an exponential, followed by a re-integration to obtain the convolved charge signal $\hat{S}(t)$:

$$\hat{S}(t) = C \sum_{t,t'=t+1} [S(t) - S(t-1)]\left(1 - \exp\left(\frac{t - t'}{\tau}\right)\right). \tag{7}$$

Here, C denotes a factor containing the fraction of charges released into the detector bulk, $S(t)$ the original (non-convolved) signal, and τ an exponential time constant describing the time scale of charge release. The equation accounts for the fact that the delayed charges are released starting from when the alpha particle penetrates the surface. The DCR rate defined in this equation is proportional to E^{obs}. It should be noted here that the DCR model in Equation (7) was tuned to match the measured effect as presented in this work. Alpha or beta surface events with other topologies, e.g., different incidence and/or energy, may not be described well.

5.2.1. Surface Alpha Events

In this section, the results of the ^{241}Am surface alpha event simulations will be discussed and compared to the measurements. The energies E_α^{true}, E_α^{obs}, and DCR rates for all simulated events are shown for negative surface charges ($\sigma = -0.1, -0.3 \times 10^{10}\,\text{e}/\text{cm}^2$) in Figure 18. The simulation predicts that with increasing radius r, the alpha population moves towards lower E_α^{obs} and DCR values. In addition, the distributions become narrower. This is in good qualitative agreement with the measurements, cf. Figure 9a. However, it should be noted here that there are differences between the spectral shapes of the measured and simulated ^{241}Am spectra. This is most likely due to the fact that the simulation framework does not fully cover all relevant effects, e.g., diffusion and self-repulsion of the charge cloud evolution were neglected. Moreover, the simplified simulation settings (e.g., simplified geometry of the experimental setup, homogeneous distribution of the surface charges, discrete simulation grid, no sophisticated electronic response, etc.) could also have an impact.

To quantify the radial dependencies predicted by the pulse shape simulations, the mean energies $\langle E_\alpha^{\text{obs}} \rangle$ and the mean DCR rates $\langle \text{DCR}_r \rangle$ were extracted from the distributions, see Figure 19. To eliminate background events (particularly the 59.5 keV gammas from ^{241}Am), only alpha events with an energy of $E_\alpha^{\text{true}} > 5.3$ MeV were selected. As for the measurements, the error bars represent the standard deviations of the distributions. The reduction of $\langle E_\alpha^{\text{obs}} \rangle$ and $\langle \text{DCR}_r \rangle$ is predicted to be stronger for a higher absolute amount of surface charges, particularly at small r, see Figure 19. A direct comparison of the predicted and measured DCR values is not meaningful, since they depend on the trace length which is different for measurement and simulation. Therefore, the simulated $\langle \text{DCR}_r \rangle$ were scaled with a constant factor which was chosen such that the absolute values roughly match. The predicted radial dependencies describe the measurement results qualitatively well. The predicted dependency of $\langle E_\alpha^{\text{obs}} \rangle$ on r describes the measurements also quantitatively for a moderate surface charge of $\sigma = -0.3 \times 10^{10}\,\text{e}/\text{cm}^2$. In contrast, the predicted $\langle \text{DCR}_r \rangle$ slightly deviate from the measured rates, particularly for $r \gtrsim 10$ mm. This might be due to the simplicity of the applied DCR model, cf. Equation (7).
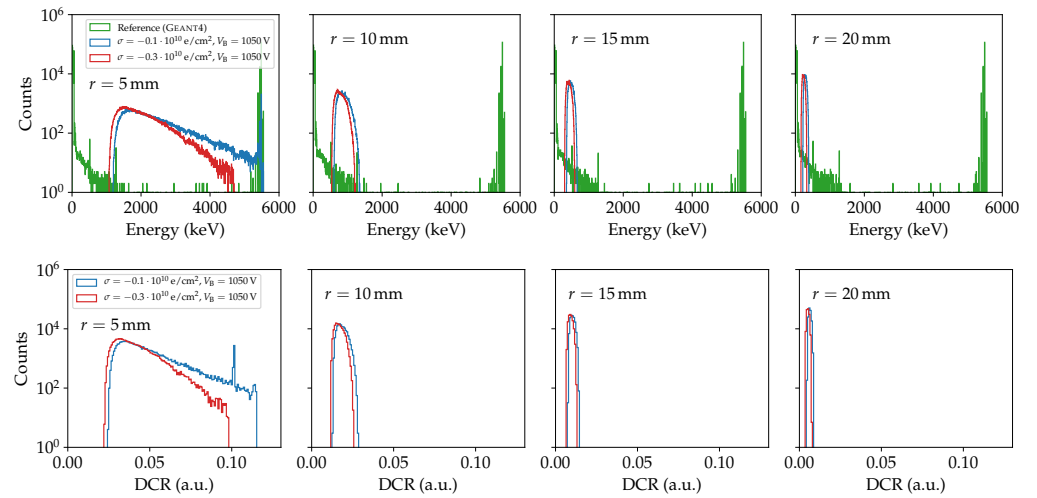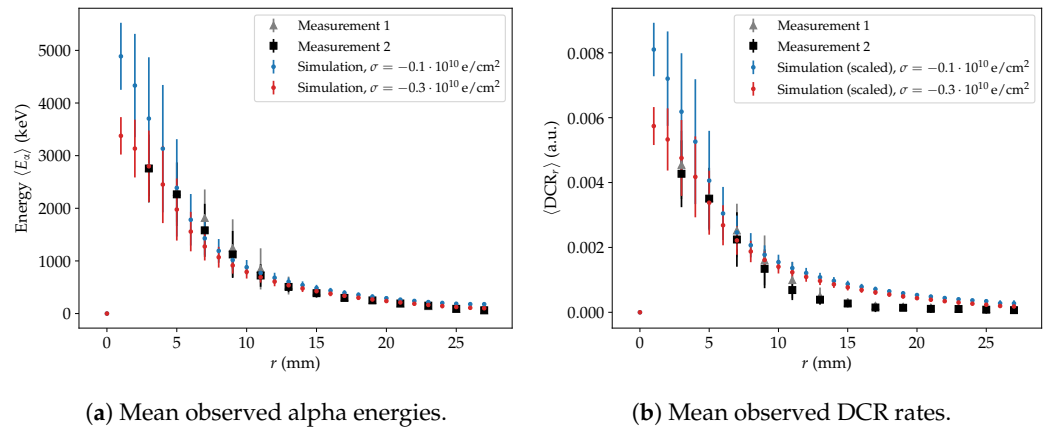
Figure 18. Simulated energy spectra E_α^{true} (GEANT4 reference, green curve), E_α^{obs} (blue and red curves) (**upper row**), and DCR distributions (**lower row**) of the ^{241}Am events at selected r. The simulated E_α^{obs} distributions are shown for negative surface charges $\sigma = -0.1, -0.3 \times 10^{10}$ e/cm^2.

(**a**) Mean observed alpha energies.

(**b**) Mean observed DCR rates.

Figure 19. Comparison of measurement to simulation: (**a**) Mean alpha energy $\langle E_\alpha^{\text{obs}} \rangle$ and (**b**) mean DCR rate $\langle \text{DCR}_{\text{r}} \rangle$. The simulation results are shown for the surface charges $\sigma = -0.1, -0.3 \times 10^{10}$ e/cm^2. The simulated DCR rates were scaled with a constant factor.

5.2.2. Surface Beta Events

The analysis of the simulated surface beta events was done in analogy to the analysis of the measurements. The simulated energy spectra in the presence of negative surface charges ($\sigma = -0.3, -0.7 \times 10^{10}$ e/cm^2) are shown in Figure 20. The predicted energy E_β^{obs} degrades with increasing r. This is in qualitative agreement with the measurements, cf. Section 4.3.2. For higher absolute surface charges, the reduction is stronger.

The dependence of the integral count rate of E_β^{obs} on r is shown in Figure 21a. The energy threshold used in the simulation had to be adjusted such that the count rates of the simulation roughly match the measured rates. This might have been necessary because of the simplified drift model which did not take diffusion and self-repulsion into account. Thus, only qualitative statements can be made. The simulation describes the increase of the count rate at small r due to the partial shadowing of the beam spot by the PTFE bar. Moreover, the simulated integral count rate decreases with r for $r > 5$ mm. However, it does not drop as steeply as the measured rate. The reduction of E_β^{obs} was also quantified in terms of the shift of the endpoints of the ^{90}Sr spectra, see Figure 21b. The spectra were fit with a seventh-order polynomial and the endpoint was approximated as for the measured spectra, cf. Section 4.3.2. While the simulation describes the measurement reasonably well

at small r, it cannot describe the measurement at large r. A better agreement between simulation and measurement is achieved for the higher value of the assumed negative surface charge. This is in contrast to the reasonable description of the alpha events when assuming a lower surface charge.
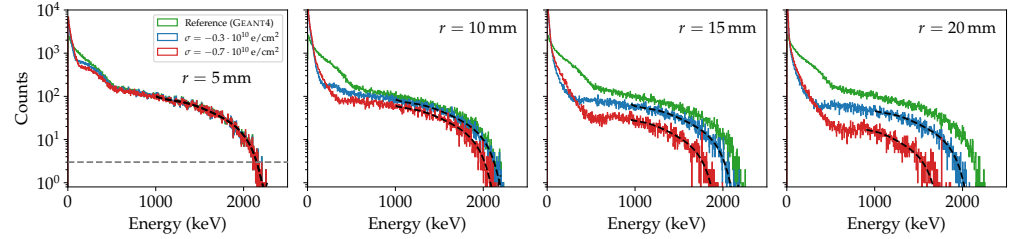

Figure 20. Distribution of E_β^{true} (GEANT4 reference, green curve) and E_β^{obs} (blue and red curves) for the simulated ^{90}Sr events at selected radial positions. The E_β^{obs} energy spectra are shown for the signal propagation in the presence of negative surface charges of $\sigma = -0.3, -0.7 \times 10^{10}$ e/cm^2. The spectra were fit with a seventh-order polynomial (black dashed lines) and the intersection with a fixed value was determined.
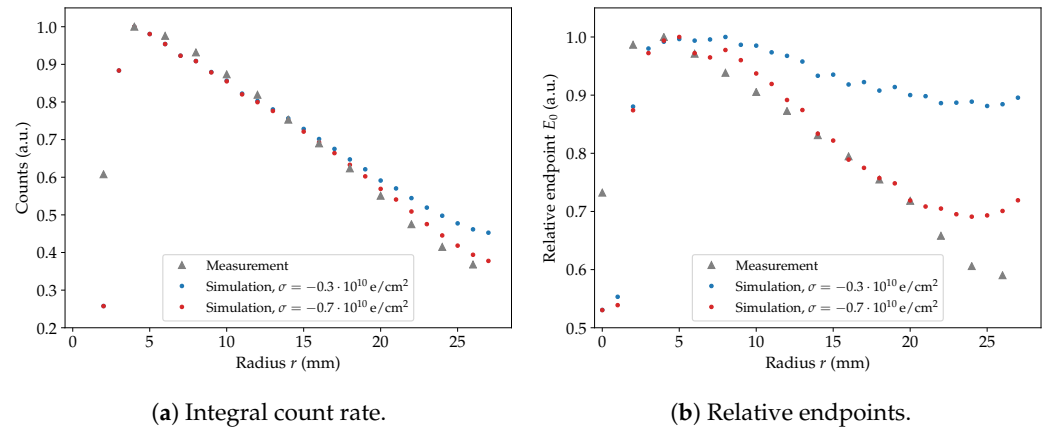

(**a**) Integral count rate.

(**b**) Relative endpoints.

Figure 21. Comparison of measurement to simulation: (**a**) Integral count rate and (**b**) relative endpoints of the ^{90}Sr E_β^{obs} energy spectra. Simulation results are shown for the surface charges $\sigma = -0.3, -0.7 \times 10^{10}$ e/cm^2.

Two event populations were observed in the radial ^{90}Sr measurements, cf. Section 4.3.2. The first population consists of events with low energies E_β^{obs}, for which the drift time decreases with increasing r. In contrast, the second population consists of events with higher energies E_β^{obs}, whose drift time increases with increasing r, see Figure 15. This is validated by the ^{90}Sr simulations as shown in Figure 22 and can be explained as follows: Events with low E_β^{true} have a small penetration depth. As discussed in Section 5.1, they are affected by surface charges and their energy E_β^{obs} is strongly reduced. In contrast, events with a high E_β^{true} generally have a higher penetration depth. These events are less sensitive to surface effects, i.e., most of the holes are collected on the p$^+$ contact.
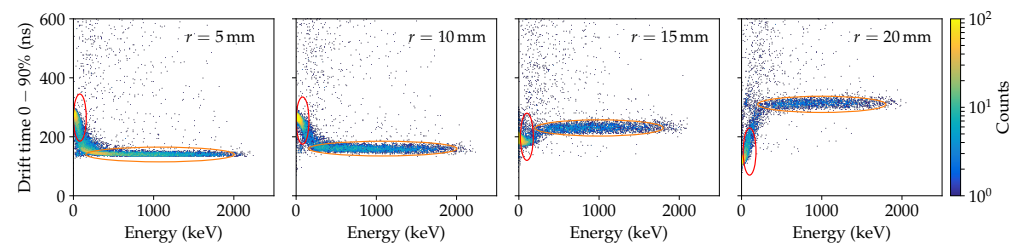
Figure 22. Predicted correlation between the drift time and energy E_β^{obs} at selected r for the simulated ^{90}Sr events. Simulation results are shown for the surface charge $\sigma = -0.3 \times 10^{10}\,\text{e}/\text{cm}^2$. The red vertical and orange horizontal ellipses in the distributions indicate two event populations.

5.3. Discussion and Outlook

The simulations carried out in the scope of this work were based on the drift models for single holes and electrons. The charges were treated as independent and the final signals were calculated as superpositions of the waveforms as expected for isolated point charges. In addition, the environment of the detector was not taken into account. The resulting simulation results were able to describe the data qualitatively well if certain surface charges were assumed. However, some quantitative differences emerged between predictions and data, and the value of the surface charge, which as was to be expected was not always the same. Two effects not taken into account in the simulations could influence the results significantly and will be discussed in the following sections.

5.3.1. Impact of Diffusion and Self-Repulsion

Thermal diffusion and Coulomb self-repulsion are two effects between the charge carriers which are expected to have a significant impact. Since these processes lead to an increase of the size of the charge cloud during its evolution, they could directly influence the fraction of charge carriers affected by surface effects.

For interactions close to the (passivated) detector surface, the transverse diffusion component and the self-repulsion are of particular importance. The transverse size of the charge cloud initially deposited increases very quickly. The effect becomes stronger for larger and denser energy depositions. In contrast, the longitudinal diffusion is less important because the longitudinal diffusivity is low in a high electric field. Thus, assuming that the field close to the surface is high enough, the charge cloud is expected to become a disk. If the expanding disk drifts parallel to the surface it can eventually intersect with the layer affected by surface effects, even if the original charge cloud did not. This will result in a "smear" of charges which are trapped close to the surface. The lower part of the charge cloud continues drifting, some part can move away and will be collected, some part might be trapped. This results in a modified charge collection behavior compared to the case of independently drifting point charges.

First attempts have been made to include these effects in pulse shape simulations. However, this is very challenging. The three-dimensional charge density distributions for both electrons and holes need to be evolved simultaneously. At each time step, a self-consistent electric field has to be recalculated. Moreover, a fine computational grid ($\mathcal{O}(20\,\mu\text{m})$) and short simulation time steps ($\mathcal{O}(0.2\,\text{ns})$) are required. From the computational point of view, these requirements are very challenging. However, work is ongoing to approximate the effects in two-dimensional calculations as well as to speed up three-dimensional calculations to the point that these effects can be included.

5.3.2. Impact of the Environment

The assumed charges on the passivated surface are not the only mechanism to change the potential and thus the field close to this surface. The environment of a detector also has an effect on the electric potential. This was investigated for the PPC detector under study using the newly developed software package `SolidStateDetectors.jl` [26]. The

package can calculate the electric potential in and around the detector taking the detector environment into account. The potential was calculated for selected configurations:

(a) bare detector, i.e., the detector surroundings were neglected, reflecting boundary conditions at the surface at $z = 0$ mm were assumed;

(b) detector mounted inside the grounded infrared shield and the detector holding structure of GALATEA;

(c) detector mounted in GALATEA plus an additional grounded plate above the passivated detector surface at a distance of 2 mm;

(d) detector submerged in LAr.

The potential Φ^{bare} of the bare detector is shown in Figure 23a, whereas the changes $\Phi^{\text{env}} - \Phi^{\text{bare}}$ caused by the different configurations are depicted in panels (b–d). The environment modifies the electric potential considerably, particularly in the region around the point contact. The grounded plate close to the passivated surface has the largest effect. It amounts to a few percent. The influence of a submersion in liquid argon is almost as strong. Such effects are on the same order of magnitude as the effects calculated for assumed moderate charges on the passivated surface. Consequently, future simulation studies to investigate detector surface effects should take the influence of the surrounding materials on the electric field into account. There is also experimental evidence that the detector under study behaved differently in a different environment [4,18].
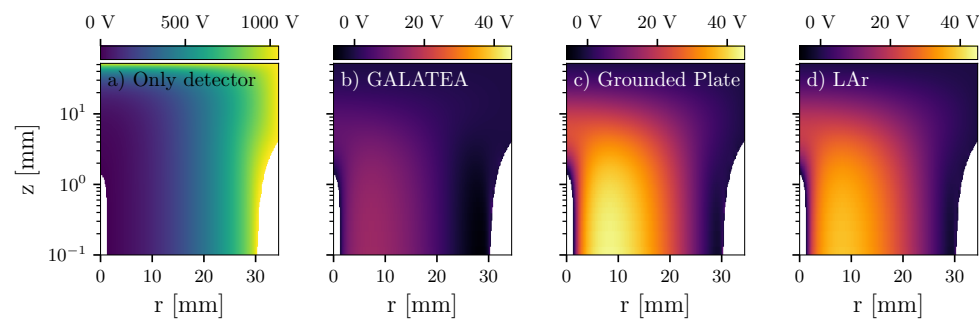

Figure 23. Electric potential of the PPC detector under study as calculated with `SolidStateDetectors.jl` [26]: (**a**) Potential Φ^{bare} as calculated for the bare detector, (**b–d**) changes in the potential $\Phi^{\text{env}} - \Phi^{\text{bare}}$ for the detector (**b**) mounted in GALATEA, (**c**) GALATEA plus a grounded plate above the passivated surface at a distance of 2 mm, and (**d**) submersed in LAr.

6. Summary and Conclusions

The response of a p-type point contact (PPC) germanium detector to alpha and beta particles was studied in detail to better understand background events as occurring in experiments searching for neutrinoless double beta decay. The results of the measurements in the vacuum test facility GALATEA demonstrate that the structure of events on the passivated detector surface can be explained by effects like surface charges. For both alpha and beta surface events, a radius-dependent reduction of the energy was observed which can be explained by assuming the presence of a negative surface charge. It was also observed that surface alpha events exhibit a delayed charge recovery (DCR) effect, which can be exploited to effectively reject such events. In former experiments like the MAJORANA DEMONSTRATOR, where alpha-induced surface events were a major contribution to the overall background, the background could be reduced by more than one order of magnitude.

In dedicated characterization measurements with beta particles, two event populations could be identified. One population could be associated with events having small penetration depths—they are affected by surface effects, whereas the waveforms of the other population with higher penetration depths were found to have no special features. No pronounced DCR effect was observed for surface beta events. Thus, the identification of beta events on the passivated surface is, if at all, only possible for a small part of the events.

An extensive simulation campaign was carried out to better understand the results of the surface characterization measurements. Pulse shape parameter maps provided insights into the impact of surface charges on quantities such as the event energy, drift time, etc. In addition, the maps revealed that the influence of a positive surface charge is much less pronounced than that of a negative surface charge. Monte Carlo event simulations in combination with pulse shape simulations were capable of reproducing the measurements qualitatively. In particular, the simulations confirmed that the measurement can be explained by the presence of a negative surface charge. This verified Monte Carlo model is also important to predict the behavior of these detectors, which will be redeployed in LEGEND-200. In this new environment, electron-induced background is expected and the fact that it cannot be identified for these detectors has to be taken into account in the analysis. The simulations will help to understand and design new detectors to be deployed in LEGEND-200 and in LEGEND-1000.

The presented measurements and corresponding simulations led to a significantly better understanding of PPC detector surface effects. This serves as a basis to better identify surface events as backgrounds to rare event searches with germanium detectors.

Author Contributions: Formal analysis, F.E., L.H., B.L. and D.C.R.; Funding acquisition, S.M.; Resources, C.G. and X.L.; Software, O.S.; Supervision, I.A., S.M. and M.W.; Validation, F.E. and L.H.; Visualization, F.E., L.H. and B.L.; Writing—original draft, F.E., L.H. and I.A.; Writing—review & editing, I.A., B.L., S.M., D.C.R. and M.W. All authors have read and agreed to the published version of the manuscript.

Institutional Review Board Statement: Not applicable.

Informed Consent Statement: Not applicable.

Data Availability Statement: Not applicable.

Conflicts of Interest: The authors declare no conflict of interest.

References

1. Dolinski, M.J.; Poon, A.W.P.; Rodejohann, W. Neutrinoless Double-Beta Decay: Status and Prospects. *Annu. Rev. Nucl. Part. Sci.* **2019**, *69*, 219–251. [CrossRef]
2. Giuliani, A.; Cadenas, J.J.; Pascoli, S.; Previtali, E.; Saakyan, R.; Schaeffner, K.; Schoenert, S. Double Beta Decay APPEC Committee Report. Report Version 3. *arXiv* **2020**, arXiv:1910.04688v2.
3. Guinn, I.S.; López-Castaño, J.M. Search for neutrinoless double-β decay in ^{76}Ge with 26 kg yr of exposure from the MAJORANA DEMONSTRATOR. *Phys. Rev. C* **2019**, *100*, 025501.
4. Arnquist, I.J.; Avignone, F.T., III; Barabash, A.S.; Barton, C.J.; Bertrand, F.E.; Blalock, E.; Bos, B.; Busch, M.; Buuck, M.; Caldwell, T.S.; et al. α-event Characterization and Rejection in Point-Contact HPGe Detectors. *arXiv* **2020**, arXiv:2006.13179.
5. Abgrall, N.; Abt, I.; Agostini, M.; Alexander, A.; Andreoiu, C.; Araujo, G.R.; Avignone, F.T., III; Bae, W.; Bakalyarov, A.; Balata, M.; et al. LEGEND-1000 Preconceptual Design Report. *arXiv* **2021**, arXiv:2107.11462.
6. Luke, P.N.; Goulding, F.; Madden, N.; Pehl, R. Low capacitance large volume shaped-field germanium detector. *IEEE Trans. Nucl. Sci.* **1989**, *36*, 926–930. [CrossRef]
7. Mertens, S.; Hegai, A.; Radford, D.C.; Abgrall, N.; Chan, Y.D.; Martin, R.D.; Poon, A.W.P.; Schmitt, C. Characterization of High Purity Germanium Point Contact Detectors with Low Net Impurity Concentration. *Nucl. Instr. Meth. Phys. Res. A* **2019**, *921*, 81–88. [CrossRef]

8. Agostini, M.; Allardt, M.; Andreotti, E.; Bakalyarov, A.M.; Balata, M.; Barabanov, I.; Heider, M.B.; Barros, N.; Baudis, L.; Bauer, C.; et al. Pulse shape discrimination for GERDA Phase I data. *Eur. Phys. J. C* **2013**, *73*, 2583. [CrossRef]

9. Edzards, F.; Willers, M.; Alborini, A.; Bombelli, L.; Fink, D.; Green, M.P.; Laubenstein, M.; Mertens, S.; Othman, G.; Radford, D.C.; et al. Investigation of ASIC-based signal readout electronics for LEGEND-1000. *J. Inst.* **2020**, *15*, P09022. [CrossRef]

10. Abgrall, N.; Abramov, A.; Abrosimov, N.; Abt, I.; Agostini, M.; Agartioglu, M.; Ajjaq, A.; Alvis, S.I.; Avignone, F.T., III; Bai, X.; et al. The Large Enriched Germanium Experiment for Neutrinoless Double Beta Decay (LEGEND). In Proceedings of the MEDEX'17 Meeting, Prague, Czech Republic, 29 May–2 June 2017.

11. Abgrall, N.; Abramov, A.; Abrosimov, N.; Abt, I.; Agostini, M.; Agartioglu, M.; Ajjaq, A.; Alvis, S.I.; Avignone, F.T., III; Bai, X.; et al. The Large Enriched Germanium Experiment for Neutrinoless $\beta\beta$ Decay: LEGEND-200 at LNGS. Proposal LNGS-P 58/18. *arXiv* **2018**. arXiv:1810.00849.

12. Myslik, J. LEGEND: The Large Enriched Germanium Experiment for Neutrinoless Double-Beta Decay. In Proceedings of the CIPANP 2018 Meeting, Palm Springs, CA, USA, 29 May–3 June 2018.

13. Agostini, M.; Bakalyarov, A.M.; Balata, M.; Barabanov, I.; Baudis, L.; Bauer, C.; Bellotti, E.; Belogurov, S.; Bettini, A.; Bezrukov, L.; et al. Modeling of GERDA Phase II data. *J. High Energy Phys.* **2020**, *3*, 139. [CrossRef]

14. Abgrall, N. [LEGEND Collaboration] The Large Enriched Germanium Experiment for Neutrinoless $\beta\beta$ Decay. LEGEND-1000 Preconceptual Design Report. Available online: https://arxiv.org/abs/2107.11462 (access on 12 October 2021).

15. Shockley, W. Currents to Conductors Induced by a Moving Point Charge. *J. Appl. Phys.* **1938**, *9*, 635–636. [CrossRef]

16. Ramo, S. Currents Induced by Electron Motion. *Proc. IRE* **1939**, *27*, 584–585. [CrossRef]

17. Radford, D.C. mjd_fieldgen and mjd_siggen Software. Available online: https://github.com/radforddc/icpc_siggen (accessed on 30 July 2020).

18. Gruszko, J. Surface Alpha Interactions in P-Type Point-Contact HPGe Detectors: Maximizing Sensitivity of ^{76}Ge Neutrinoless Double-Beta Decay Searches. Ph.D. Thesis, University of Washington, Seattle, WA, USA, 2017.

19. Cooper, R.J.; Radford, D.C.; Hull, E.; Lagergren, K.; Mullowney, P.; Lin, M.C.; Paul, K.; Athens, C.; Loh, M. Effect of a surface channel on the performance of a P-type Point Contact HPGe detector. *Nucl. Instr. Meth. Phys. Res. A* **2012**, *680*, 48–55. [CrossRef]

20. Abt, I.; Caldwell, A.; Dönmez, B.; Garbini, L.; Irlbeck, S.; Majorovits, B.; Palermo, M.; Schulz, O.; Seitz, H.; Stelzer, F. The GALATEA test-facility for high purity germanium detectors. *Nucl. Instr. Meth. Phys. Res. A* **2015**, *782*, 56–62. [CrossRef]

21. Irlbeck, S. The GALATEA Test Facility and a First Study of α-induced Surface Events in a Germanium Detector. Ph.D. Thesis, Ludwig-Maximilians-Universität München, Munich, Germany, 2014.

22. Aalseth, C.E.; Abgrall, N.; Aguayo, E.; Alvis, S.I.; Amman, M.; Arnquist, I.J.; Avignone, F.T., III; Back, H.O.; Barabash, A.S.; Barbeau, P.S.; et al. Search for Neutrinoless Double-β Decay in ^{76}Ge with the Majorana Demonstrator. *Phys. Rev. Lett.* **2018**, *120*, 132502. [CrossRef] [PubMed]

23. Edzards, F. Characterization of Point Contact Germanium Detectors and Development of Signal Readout Electronics for LEGEND. Ph.D. Thesis, Technical University of Munich, Munich, Germany, 2021.

24. Mullowney, P.; Lin, M.C.; Paul, K.; Ahrens, C.; Loh, M.; Cooper, R.J.; Radford, D.C.; Hull, E. Computational models of germanium point contact detectors. *Nucl. Instr. Meth. Phys. Res. A* **2012**, *662*, 33–44. [CrossRef]

25. Wagner, V.E. Pulse Shape Analysis for the GERDA Experiment to Set a New Limit on the Half-life of $0\nu\beta\beta$ Decay of ^{76}Ge. Ph.D. Thesis, Ruperto-Carola-University of Heidelberg, Heidelberg, Germany, 2017.

26. Abt, I.; Fischer, F.; Hagemann, F.; Hauertmann, L.; Schulz, O.; Schuster, M.; Zsigmond, A.J. Simulation of semiconductor detectors in 3D with SolidStateDetectors.jl. *arXiv* **2021**, arXiv:2104.00109.